processes

MDPI

*Article*

# Design of Continuous Fixed Plate Photo-Fenton Reactor Based on $Fe_3O_4/TiO_2@Al_2SiO_5$ Fiber Board Photocatalyst and Application in Tetracycline Hydrochloride Degradation

**Xiaodan Yu *, Yang Cui and Qiancheng Ji**

Key Laboratory of Songliao Aquatic Environment, Ministry of Education, Jilin Jianzhu University, Changchun 130118, China
* Correspondence: yuxiaodan061213@163.com

**Abstract**

To address the limitations of traditional photo-Fenton reactions in antibiotic wastewater treatment, this study designed a continuous flat-plate photo-Fenton reactor based on the $Fe_3O_4/TiO_2@Al_2SiO_5$ fiberboard photocatalyst and applied it to the degradation of tetracycline HCl (TCH). The supported catalyst $Fe_3O_4/TiO_2@Al_2SiO_5$ was prepared via a calcination method, using the $Al_2SiO_5$ fiberboard as the carrier. This not only effectively addresses the issue of catalyst recovery but also enhances the dispersion and stability of the $Fe_3O_4/TiO_2$ catalyst as a support. Moreover, the catalyst mainly exhibited an amorphous structure. $TiO_2$ and $Fe_3O_4$ were successfully loaded onto the surface of the carrier. The operating parameters of the reactor were systematically optimized, and the optimal conditions were determined as follows: TCH influent concentration of 50 mg/L, hydraulic retention time (HRT) of 120 min, initial pH of 4.5, $H_2O_2$ dosage of 10 mmol/L, and ultraviolet (UV) light intensity of 2.36 kW/m$^3$. Under these conditions, the TCH removal efficiency could reach over 90%. Active species trapping experiments indicated that hydroxyl radicals (•OH) were the main active substances responsible for TCH degradation. With the assistance of HPLC-MS/MS and GC-MS analyses, 19 types of degradation intermediates were identified. It was proposed that the TCH degradation pathway mainly included •OH-mediated hydroxylation addition reactions and demethylation reactions initiated by •OH and $h^+$. The toxicity assessment showed that the toxicity of the degradation intermediates gradually decreased with the progress of the reaction. This reactor features high efficiency, stability, and easy operation, providing a feasible solution for the large-scale treatment of antibiotic wastewater.

**Keywords:** $Fe_3O_4/TiO_2@Al_2SiO_5$; photo-Fenton reactor; TCH; $H_2O_2$



Academic Editors: Manuel J. Chinchillas-Chinchillas, Priscy Alfredo Luque Morales and Horacio Edgardo Garrafa-Gálvez

Received: 5 November 2025
Revised: 19 November 2025
Accepted: 25 November 2025
Published: 26 November 2025

**Citation:** Yu, X.; Cui, Y.; Ji, Q. Design of Continuous Fixed Plate Photo-Fenton Reactor Based on $Fe_3O_4/TiO_2@Al_2SiO_5$ Fiber Board Photocatalyst and Application in Tetracycline Hydrochloride Degradation. *Processes* **2025**, *13*, 3824. https://doi.org/10.3390/pr13123824



## 1. Introduction

Recently, due to the widespread use of antibiotics and a large number of residual antibiotics entering the water and soil environment, antibiotic pollutants cause endless harm to the ecological environment [1,2]. Therefore, the development of water treatment processes for antibiotic pollutants is of great significance for environmental protection and the healthy development of human society. The traditional methods for removing antibiotics from water include physical adsorption [3], biological degradation [4], and advanced oxidation processes (AOPs) [5]. Physical adsorption has a wide range of applications [6], but the adsorption capacity of the adsorbent is prone to saturation [7], and there

is a risk of secondary pollution. The cost of biodegradation is low, but microorganisms are prone to developing resistance and have demanding living conditions [8]. Therefore, currently, the advanced oxidation process is commonly used for the degradation of antibiotics. Radical-based advanced oxidation processes (AOPs) yielded a good catalytic effect on the degradation of antibiotic wastewater by the activation of peroxodisulfate (PDS) [9], peroxymonosulfate (PMS) [10], and hydrogen peroxide ($H_2O_2$) [11], etc. Among them, photo-Fenton reactions have gained wide attention because of their simple operation, being environmentally friendly, and low cost. However, some drawbacks such as acid environments and a low $Fe^{3+}/Fe^{2+}$ cycle rate hinder the practical applications [12].

To overcome the aforementioned limitations of photo-Fenton reactions, some studies have shown that the introduction of semiconductor photocatalytic materials (e.g., $BiVO_4$, $TiO_2$) to photo-Fenton not only yielded a good catalytic effect on the degradation of wastewater but also helps solve some problems associated with photo-Fenton systems [13,14]. Upon light irradiation, hole-electron pairs are formed on the surface of photocatalytic materials (Equation (1)). $Fe^{3+}$ in the Fenton reagent acts as an electron acceptor to capture photoexcited electrons and is effectively reduced (Equation (2)). The cycle rate of $Fe^{3+}/Fe^{2+}$ is improved so that more hydroxyl radicals are generated in the system, and the treatment effect is obviously improved. At the same time, $Fe^{3+}$ acts as an electron capture agent to inhibit the recombination of $TiO_2$ photogenerated holes and electrons and also improves the quantum efficiency of photocatalysis [15,16]. For example, Xu et al. [15] developed $BiVO_4$/Fh semiconductors as Fenton composite catalysts by modifying the structure and surface of natural nano-mineral materials. The results showed that $BiVO_4$ promotes the decomposition of $H_2O_2$, and the high concentration of $Fe^{2+}$ in the system indicates that the photogenerated electrons generated by $BiVO_4$ promote $Fe^{3+}/Fe^{2+}$ conversion, thereby improving the decomposition efficiency of $H_2O_2$, rather than the degradation of $H_2O_2$ by $BiVO_4$. Furthermore, Deng et al. [17] found that the P-type semiconductor is not suitable for coupling with the Fenton reagent. The hole concentration of P-type semiconductors is much greater than the free electron concentration, and holes will consume $H_2O_2$ in the system, which also leads to a decrease in catalytic efficiency due to the reduction in holes.

$$\text{Semiconductor} \xrightarrow{h\nu} {e_{CB}}^- + {h_{VB}}^- \quad (1)$$

$$Fe^{3+} + {e_{CB}}^- \rightarrow Fe^{2+} \quad (2)$$

At present, the research on photo-Fenton or photocatalysis is mainly limited to the laboratory. The design and development of a heterogeneous photocatalytic reactor with high efficiency, good stability, and operation simplicity is a problem that needs to be addressed for large-scale application. According to the form of catalysts, heterogeneous photocatalytic reactors can be divided into suspension reactors [18] and supported reactors [19]. Suspension reactors have the advantages of high mass transfer efficiency, good photon absorption performance, high degradation efficiency of pollutants, and simple structure [20]. However, there is a problem of catalyst recovery in practical applications, and they are mostly designed as sequencing batch reactors. In a supported reactor, the catalyst is fixed or attached to a carrier such as ceramic, glass, zeolite, etc., and then placed in the reactor, thus avoiding the problem of catalyst recovery, and the reactor can also be operated continuously. In addition, according to the bed state of the reactor, they can be divided into fluidized-bed and fixed-bed photocatalytic reactors. The catalyst in the fluidized bed photocatalytic reactor is always in a flowing state, which improves the specific surface area of the catalyst and the utilization rate of light to a certain extent. However, due to the serious back-mixing of materials and particle wear, it is necessary to increase the recovery and dust collection devices. This makes its internal components and operations complex.

The fixed-bed photocatalytic reactor solves the problem of material back-mixing very well. The fluid reacts through the bed formed by the catalyst fixed on the carrier, the mechanical loss of the catalyst is small, and the structure of the reactor is simple. At present, fixed-bed photocatalytic reactors can be divided into shallow pool reactors, tubular reactors, flat-plate reactors, and optical fiber bundle photochemical reactors according to their structure and shape. Among many fixed-bed reactors, plate photocatalytic reactor has attracted more and more attention because of its high light utilization and simple structure.

So far, the synergies of Fe and Ti have been shown to efficiently activate the degradation of pollutants by UV-Fenton, but the design and development of a heterogeneous photocatalytic reactor with high efficiency, good stability, and operation simplicity is a problem that need to be addressed for large-scale application. Therefore, in this study, $Fe_3O_4/TiO_2@Al_2SiO_5$ prepared using $Al_2SiO_5$ fiber as the carrier was fabricated by the calcination method and applied to the plate fixed-bed continuous flow reactor. The efficiency of $Fe_3O_4/TiO_2@Al_2SiO_5$ for the degradation of pollutants by fixed plate UV-Fenton reactor was tested by taking TCH as the target contaminant. The operation parameters of the process were also optimized. The reactive oxygen species (ROS) in the $Fe_3O_4/TiO_2@Al_2SiO$/UV-Fenton system were analyzed through radical quenching experiments. Combining the intermediate products of TCH degradation detected by HPLC-MS/MS and GC-MS, the possible degradation pathways of TCH were proposed. By studying the degradation mechanism of TCH in the $Fe_3O_4/TiO_2@Al_2SiO$/UV-Fenton system, the electronic cycling and synergistic effect were explored. The toxicity of the degradation products was evaluated using the toxicity assessment soft tool (ECOSAR). This study provided valuable approaches for developing efficient catalysts and designed a novel plate fixed-bed continuous flow UV-Fenton reactor, achieving immobilization of the $Fe_3O_4/TiO_2$ composite catalyst and its efficient degradation of TCH. The findings provide valuable guidance for the industrial application of the catalyst.

## 2. Materials and Methods

### *2.1. Chemicals and Materials*

All chemicals used in this study were analytical-grade reagents and were used without further purification. Tetracycline (TC) HCl ($C_{22}H_{24}N_2O_8$ HCl) was obtained from Sigma (Sigma–Aldrich Chemical Co., Shanghai, China). Sodium thiosulfate pentahydrate ($Na_2S_2O_3{\cdot}5H_2O$), Ferric chloride ($FeCl_3{\bullet}6H_2O$), Ferrous chloride ($FeCl_2{\bullet}4H_2O$), sulfuric acid ($H_2SO_4$), Sodium hydroxide (NaOH), tetrabutyl titanate (TBT), t-BuOH, p-benzoquinone (BQ), sodium azide and ammonium oxalate and hydrogen peroxide ($H_2O_2$) 30% were purchased from Shenyang East China Reagent Plant, Shenyang, China. The $Al_2SiO_5$ board was purchased by Hebei Fuluda Company, Baoding, China. All solutions were prepared in deionized water.

### *2.2. Preparation and Characterization of $Fe_3O_4/TiO_2@Al_2SiO_5$*

The $Fe_3O_4/TiO_2$-coated $Al_2SiO_5$ fiberboard ($Fe_3O_4/TiO_2@Al_2SiO_5$) was fabricated using the calcination method. Firstly, a certain amount of $FeCl_3{\bullet}6H_2O$ and $FeCl_2{\bullet}4H_2O$ was dissolved in 100 mL distilled water. And then, 30 mL $NH_3{\bullet}H_2O$ was added to a water bath at 60 °C and continuously stirred for 40 min to obtain a solution containing $Fe_3O_4$. An amount of this solution was taken and dropped on the $Al_2SiO_5$ fiberboard. After drying for 12 h, 5 mL of tetrabutyl titanate sol–gel was evenly dropped onto the surface, and finally the precursor was calcined at 300 °C in the synthesis atmosphere (90% $N_2$, 10% $O_2$) for 1 h (10 °C/min), and then heated to 550 °C at the same rate for 4 h. Five $Fe_3O_4/TiO_2@Al_2SiO_5$ were prepared with different $Fe_3O_4$ loading dosages (0.1 g/L, 0.25 g/L, 0.5 g/L and 0.75 g/L).

The X-ray diffraction (XRD) patterns of all powders were obtained on a Rigaku D/Max 2550 diffractometer (Rigaku Corporation, Tokyo, Japan) using a Cu Kα radiation source (ƙ= 1.54056) at a scan rate of 10° $min^{-1}$ to determine the crystal phase of the obtained samples. The acceleration voltage and the applied current were 3 kV and 20 mA, respectively. The surface morphology was characterized by field-emission scanning electron microscopy (FE-SEM, NOVA-230, FEI, Hillsboro, OR, USA). The chemical composition was analyzed using X-ray photoelectron spectroscopy (XPS, ESCA LAB 220-XL, Al Kα radiation XPS, Thermo Fisher Scientific 250Xi, Waltham, MA, USA). The degradation intermediate products of TCH were detected using ultra-high performance liquid chromatography-tandem mass spectrometry (UPLC-MS/MS, Agilent1100 Agilent, Santa Clara, CA, USA) and Gas Chromatography-Mass Spectrometry (GC-MS-QP2010 Plus, Tokyo, Japan).

### *2.3. Setting Up of the Reactor and Analytical Methods*

The overall structure of the designated plate fixed-bed UV-Fenton reactor is shown in Figure 1. The main material of the reactor is plexiglass. In the radial direction, it is divided into five areas: the lowest layer and the uppermost layer are water inlet and water outlet area, respectively, and the middle layers are the main reaction areas. Each reaction area is loaded with $Fe_3O_4/TiO_2@Al_2SiO_5$. The samples are separated by $Fe_3O_4/TiO_2@Al_2SiO_5$ fiberboard, the middle of each reaction zone has a 4 W (8 W, 15 W) UV lamp as a light source, and an aeration device is installed at the bottom of the reactor. The operation mode of the gas and liquid phases in the reactor is shown in Figure 1. After entering the reactor from the bottom, the gas flow is completely mixed with the solution. The gas flow is used as the driving force to raise the water flow. After the degradation reaction, the liquids are released through the effluent zone.

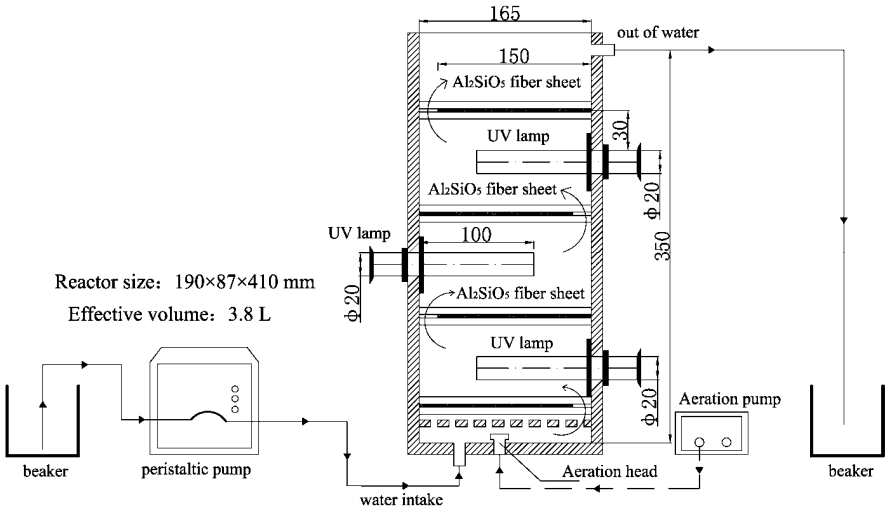


**Figure 1.** A schematic diagram of the plate fixed-bed UV-Fenton reactor.

The schematic diagram of the experiment is to mix 3.8 L of simulated TCH wastewater with $H_2O_2$. If the hydraulic retention time is calculated as 2 h, the influent flow rate is about 0.032 L/min, and aeration at a ventilation rate of 25 mL/min, timing is started when the UV lamp is turned on, and samples are collected and measured at certain intervals.

The absorbance of TCH was measured at 375 nm via an ultraviolet-visible spectrophotometer (752, Shanghai Shunyu Instrument Co., Ltd., Shanghai, China). The degradation intermediate products of TCH were detected using ultra-high performance liquid chromatography-tandem mass spectrometry (UPLC-MS/MS) and Gas Chromatography-Mass Spectrometry (GC-MS).

## 3. Results and Discussion

### *3.1. Characterization Results*

To determine the phase composition of the loaded catalyst, XRD analysis was carried out on the $Al_2SiO_5$ fiberboard. Figure 2a is the XRD patterns of $Al_2SiO_5$ fiberboard before and after loading. It is observed that there is no obvious diffraction peak in the XRD of $Al_2SiO_5$ fiberboard before loading, indicating that the obtained fiberboard is an amorphous phase. After $Fe_3O_4$ and $TiO_2$ were loaded, strong X-ray diffraction peaks appeared in the XRD pattern of the fiberboard. The sample shows distinct diffraction peaks at 2θ values of 30.12°, 35.48°, 43.12°, 53.50°, 57.03°, 62.62°, and 74.09°. Analyzed using the standard card $Fe_3O_4$ (PDF#88-0866), this sample is of the tetragonal crystal system and belongs to magnetite. Through analysis, it is concluded that the peaks belong to the characterization of $Fe_3O_4$. However, due to the small amount of $TiO_2$, no corresponding characteristic peak was found. Therefore, the phase of $Al_2SiO_5$ fiberboard catalyst is mainly an amorphous phase.

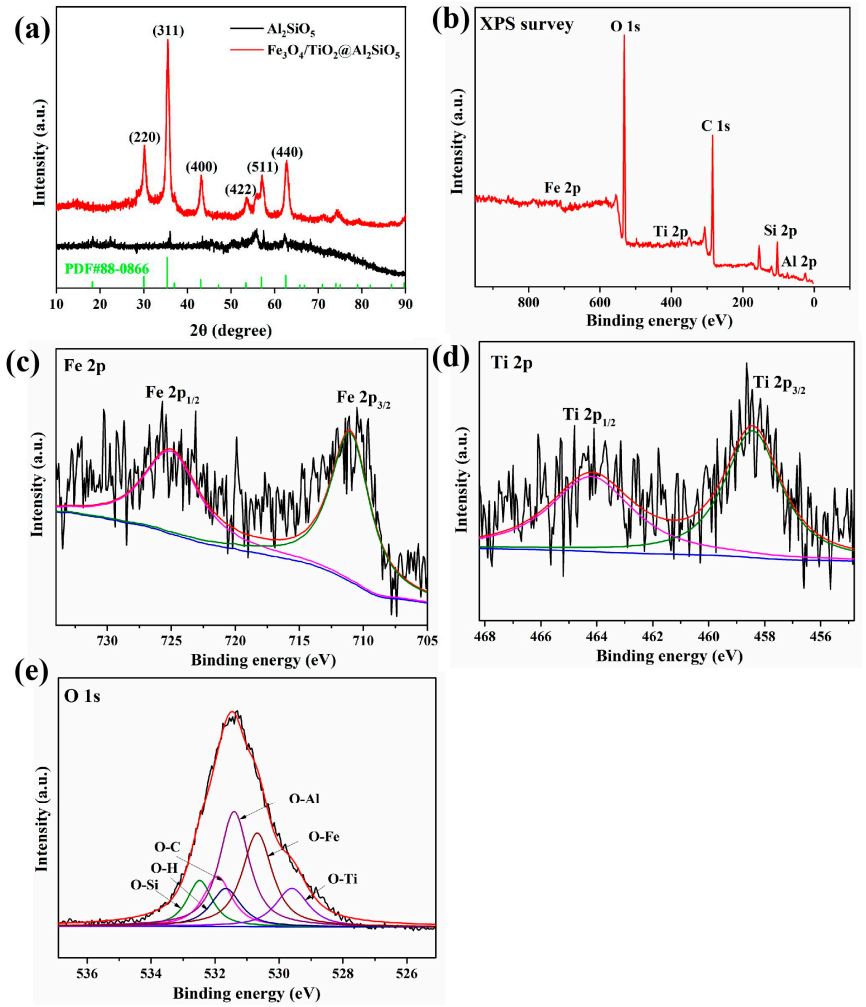


**Figure 2.** (**a**) XRD pattern of $Al_2SiO_5$ fiberboard and $Fe_3O_4/TiO_2@Al_2SiO_5$; (**b**) XPS survey spectrum of $Fe_3O_4/TiO_2@Al_2SiO_5$; (**c**) Fe 2p; (**d**) Ti 2p and (**e**) O 1s.

Since certain components within the obtained $Fe_3O_4/TiO_2@Al_2SiO_5$ fiberboard catalyst samples exist in an amorphous phase, their phase composition cannot be determined through the XRD analysis. To further investigate the mainly amorphous phase of the catalyst, XPS analysis was employed to examine its chemical composition and the chemical states of each element. The full-scan survey in Figure 2b showed that the sample is mainly

composed of Fe, O, Ti, C, Si, and Al. Among them Si, Al, and O elements constitute $Al_2SiO_5$ fiberboard, and Fe, O, and Ti elements are the constituent elements of $Fe_3O_4$ and $TiO_2$.

Simultaneously, high-resolution XPS spectroscopy was performed on Fe 2p, Ti 2p, and O 1s. The high-resolution XPS spectrum of Fe 2p, as shown in Figure 2c, exhibits peaks at binding energies of 710.9 eV and 725.8 eV, corresponding to Fe $2p_{3/2}$ and Fe $2p_{1/2}$, respectively [21]. Following Gaussian–Lorentzian deconvolution (peak separation), the Fe $2p_{3/2}$ and Fe $2p_{1/2}$ peaks were fitted to $Fe^{3+}$ (726.2 eV and 712.2 eV) and $Fe^{2+}$ (724.3 eV and 710.2 eV), respectively. The $Fe^{3+}$ to $Fe^{2+}$ ratio was approximately 2:1, which is consistent with the binding energies reported for $Fe_3O_4$ in the literature. The high-resolution XPS spectrum of Ti 2p in Figure 2d shows $Ti^{4+}$ $2p_{3/2}$ and $Ti^{4+}$ $2p_{1/2}$ binding energies of 464.3 eV and 458.5 eV, respectively, with a peak separation of 5.8 eV. Comparison with standard spectra indicates these values are typical for $Ti^{4+}$ in $TiO_2$. The high-resolution XPS spectrum of O 1s in Figure 2e was fitted into six peaks with binding energies of 532.8 eV, 532.2 eV, 531.6 eV, 531.5 eV, 530.1 eV, and 529.6 eV. The 530.1 eV and 529.6 eV peaks correspond to the O-Fe bond in $Fe_3O_4$ and the O-Ti bond in $TiO_2$, respectively, representing lattice oxygen [22,23]. The peaks at 531.6 eV and 532.2 eV correspond to the O-H bond and O-C bond, respectively [24]. The binding energies of 532.8 eV and 531.5 eV correspond to the O-Si and O-Al bonds in the $Al_2SiO_5$ carrier, respectively. It is evident that the $Al_2SiO_5$ fiberboard carrier has not altered the chemical composition or elemental state of $Fe_3O_4$ and $TiO_2$.

The surface morphology of the $Al_2SiO_5$ fiberboard was characterized by SEM (Figure 3a). It was observed that the $Al_2SiO_5$ fiberboard carrier exhibited a filamentous structure with a rough and uneven surface, making them suitable for loading powdered catalysts. The diameter of the filaments is approximately 10 μm (Figure 3a). Figure 3b shows the SEM image of $Fe_3O_4/TiO_2@Al_2SiO_5$ fiberboard. The surface of the loaded $Al_2SiO_5$ fibers appears even rougher. The enlarged inset in Figure 3b reveals nanoscale $Fe_3O_4$ particles loaded onto the surface of the $Al_2SiO_5$ fibers and $TiO_2$ with lamellar structure is coated on the $Al_2SiO_5$ fibers surface. As shown in Figure 3c, Si, Al, O, Fe, and Ti could be detected. And the elements Si, Al and O are the main constituents of the fiberboard and formed the skeleton structure of the sample. The elements Fe, Ti, and O are highly uniformly distributed on the surface of $Fe_3O_4/TiO_2@Al_2SiO_5$. Additionally, the EDX energy spectrum of the sample reveals the presence of three Fe, Ti, and O elements (Figure 3e). The Au element is attributed to the gold spraying pretreatment performed during SEM. Signal peaks at energies of 0.41 and 4.52 keV correspond to the Ti element in $TiO_2$, while peaks at 0.72, 6.44, and 7.06 keV correspond to Fe in $Fe_3O_4$, while the peak at 0.52 keV corresponds to O element. Compared to $Al_2SiO_5$ Figure 3d, the peak area ratio of O in $Fe_3O_4/TiO_2@Al_2SiO_5$ shows a significant increase, originating from oxygen in $Fe_3O_4/TiO_2$ and adsorbed oxygen. The percentages of C, O, Al, and Si in the $Al_2SiO_5$ fiberboard are 23.99%, 57.17%, 6.53%, and 12.31%, respectively. The proportions of C, O, Al, Si, Ti, and Fe in $Fe_3O_4/TiO_2@Al_2SiO_5$ are 39.88%, 41.96%, 4.61%, 6.22%, 0.13%, and 7.21%, respectively. The presence of C might be due to the fact that there was C in the organic ligands during the synthesis process, and the synthesis process did not thoroughly remove it, resulting in residual C. Alternatively, it could be because $CO_2$ was present in the testing environment. The low content of Ti is due to the small amount of Ti used in the doping process.

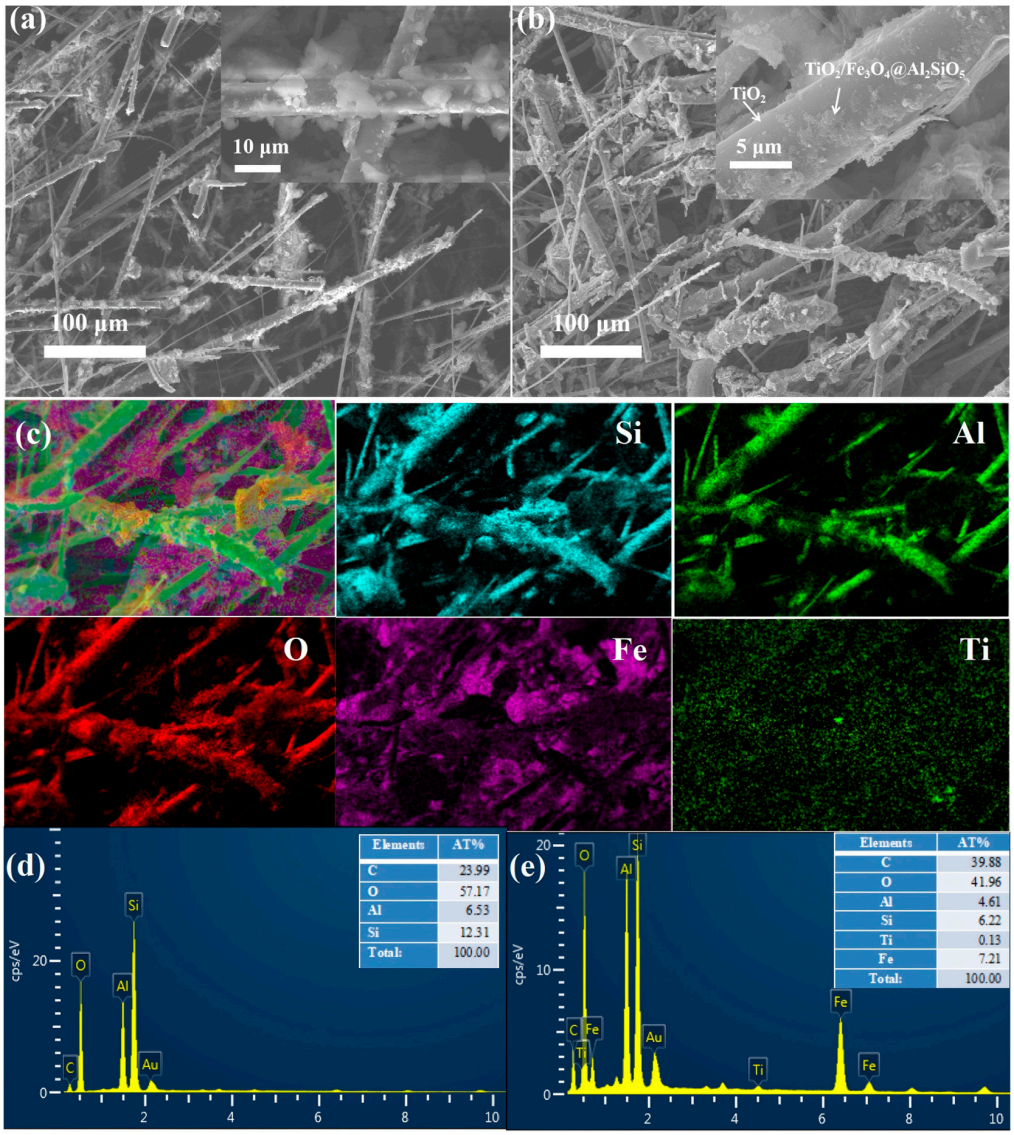


**Figure 3.** SEM images of (**a**) $Al_2SiO_5$ fiberboard and (**b**) $Fe_3O_4/TiO_2@Al_2SiO_5$; (**c**) Elemental mapping of Si, Al, O, Fe, Ti on $TiO_2/Fe_3O_4@$ $Al_2SiO_5$; (**d**) The EDS spectra of $Al_2SiO_5$ fiberboard (**e**) $Fe_3O_4/TiO_2@Al_2SiO_5$.

### *3.2. Optimization of Operating Parameters for TCH Degradation in the Plate Fixed-Bed Reactor*

#### 3.2.1. Optimization of Loading Dosage

The effect of catalyst dosage was investigated as the amount of catalyst used has a certain effect on the degradation of TCH. The results are shown in Figure 4a. We can see that the removal rate of TCH gradually increases with the increase in load of $Fe_3O_4/TiO_2@Al_2SiO_5$. For catalyst loading of 0.1 g/L, 0.25 g/L, 0.5 g/L, and 0.75 g/L, the removal rates of TCH after 120 min were 74.5%, 80.5%, 93.5%, and 94%, respectively. As shown in Figure 4b, at different initial concentrations, $\ln(C/C_0)$ shows a good linear relationship with time, and the fitting equation $R^2$ is close to 1. Moreover, when the loading dosage is 0.75 g/L, the reaction rate is the fastest, which is consistent with Figure 4a.The result indicates that an increase in the catalyst loading into the reaction increases the reaction area of the heterogeneous Fenton reaction, which in turn increases the active sites on the catalyst surface, and improves the efficiency of the process [25]. However, as the catalyst dosage continued to increase to 0.75 g/L, the TCH removal rate improved by only 1.5%. Therefore, to achieve cost-effective operation, the catalyst dosage should be maintained at 0.5 g/L.

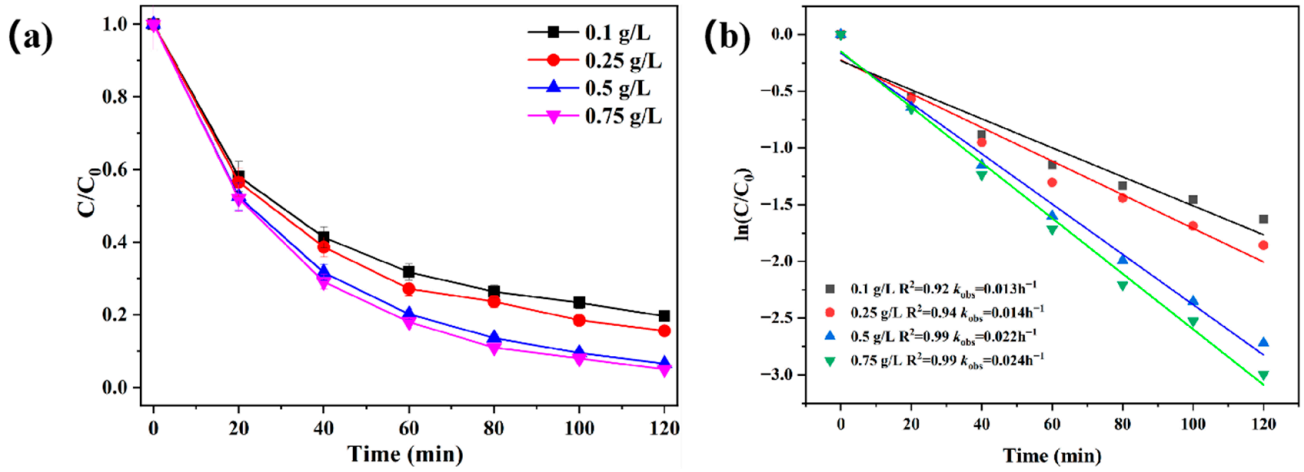


**Figure 4.** (**a**) The degradation of TCH; (**b**) Reactivity kinetics. Effect of loading dosage on TCH catalytic activity of catalyst. Experimental conditions: initial pH = 4.5 (without adjustment), $H_2O_2$ = 10 mmol/L, HRT = 2 h, $[TCH]_0$ = 50 mg/L, and T = 25 ± 1 °C.

### 3.2.2. Effect of pH Value on the Degradation

The pH of a solution is a very important factor affecting the treatment effect of the plate fixed-bed UV-Fenton reactor. About 0.1 M $H_2SO_4$ and 0.1 M NaOH solutions were used to adjust the pH of the TCH solution. The result of the effect of the initial pH on TCH degradation is shown in Figure 5a. For pH values of 3.0, 5.0, 7.0, and 9.0, the degradation rate of TCH increases first and then decreases with the increase in pH value. The removal rates are 90.5%, 93.5%, 78.3%, and 69.3%, respectively, for pH 3.0, 5.0, 7.0, and 9.0. As shown in Figure 5b, at different pH values, the linear relationship between $\ln(C/C_0)$ and time conforms to the first-order kinetic model. The reaction is in accordance with the first-order kinetic model at different pH values. When pH = 5, the reaction rate is the fastest, further indicating that pH = 5 is the optimal pH for the reaction. In previous studies [26], it can be found that the UV-Fenton reaction in the beaker test could be operated at a wider pH range, which is mainly related to the treatment method. The beaker test belongs to the sequencing batch reaction, and the organic acids generated in the system first gradually increased and then gradually decreased with the progress of the reaction. For the continuous flow reactor, the intermediate metabolites (organic acids) generated in the system will be discharged from the system with the effluent, resulting in a slow drop in pH value in the system (Table 1).

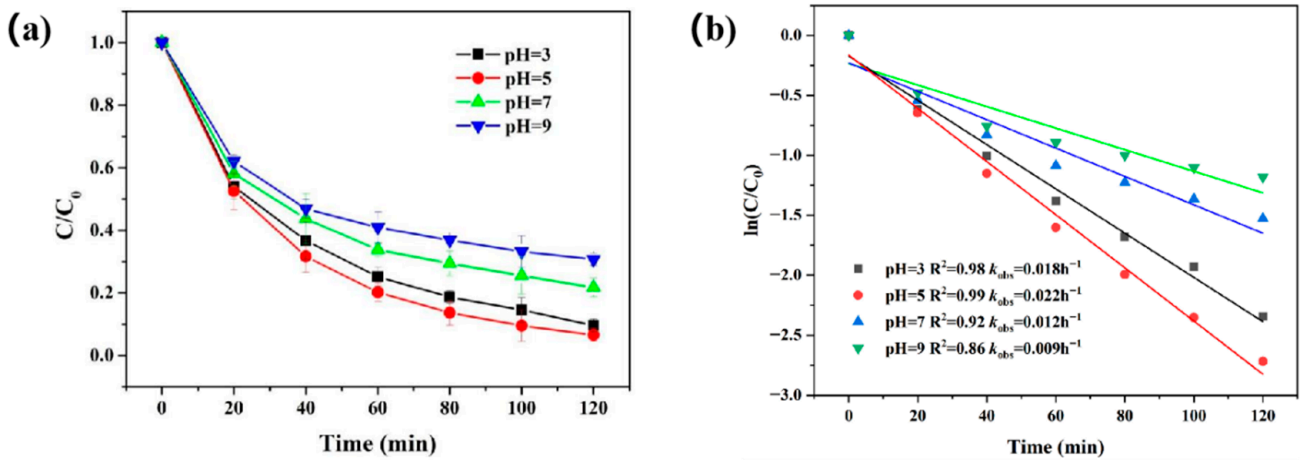


**Figure 5.** (**a**) The degradation of TCH; (**b**) Reactivity kinetics. Effect of initial pH on TCH degradation. (Experiment conditions: TCH concentration = 50 mg/L, $H_2O_2$ concentration = 10 mmol/L, catalyst dosage = 0.5 g/L, HRT = 120 min, irradiation = 6 W UV lamps, Temperature = 25 °C).

**Table 1.** Variation in solution pH on TCH degradation in the plate fixed-bed UV-Fenton reactor under different initial pH values.

| Time (min) | pH | | | |
|---|---|---|---|---|
| 0 | 3.02 | 5.10 | 7.00 | 9.00 |
| 20 | 3.00 | 4.70 | 6.52 | 7.55 |
| 40 | 3.01 | 4.67 | 6.41 | 7.45 |
| 60 | 2.98 | 4.52 | 6.30 | 7.35 |
| 80 | 2.97 | 4.37 | 6.24 | 7.25 |
| 100 | 2.98 | 4.35 | 6.15 | 7.18 |
| 120 | 2.98 | 4.24 | 6.07 | 7.17 |

### 3.2.3. Effect of $H_2O_2$ Concentration

The main source of the hydroxyl radical in the UV-Fenton system is from the decomposition of $H_2O_2$. The dosage of $H_2O_2$ will not only affect the production of the hydroxyl radical but will also affect the project cost during practical application. The dosage or amount of $H_2O_2$ is therefore vital to the process and hence it is investigated in this study for TCH degradation. The results are presented in Figure 6a. We can see that the change in concentration of $H_2O_2$ from 5 mmol/L to 20 mmol/L first shows an increase in the removal efficiency of TCH and then a decrease with more concentration of $H_2O_2$. After 120 min of the reaction, the initial concentration of $H_2O_2$ from 5 mmol/L, 10 mmol/L, and 20 mmol/L resulted in a TCH removal efficiency of 63.2%, 93.4% and 78.5%, respectively. It can be concluded from this result that the best dosage of $H_2O_2$ in the plate fixed-bed UV-Fenton reactor system is 10 mmol/L. As shown in Figure 6b, at different $H_2O_2$ concentration, the linear relationship between $\ln(C/C_0)$ and time conforms to the first-order kinetic model. This result indicates that the higher the dosage of $H_2O_2$, the more the hydroxyl radical produced in the system and the better the removal efficiency. A further increase in the $H_2O_2$ dosage would compete for active species resulting in a decrease in the removal rate of TCH in the reaction system and also unnecessary waste of $H_2O_2$ leading to a higher cost.

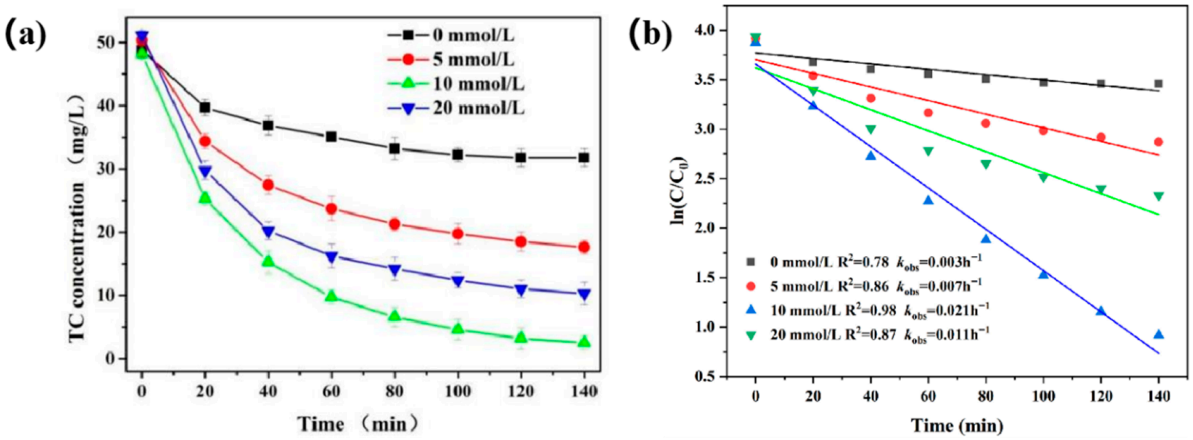


**Figure 6.** (**a**) The degradation of TCH; (**b**) Reactivity kinetics. Effect of $H_2O_2$ concentration on TCH degradation. Experiment conditions: TCH concentration = 50 mg/L, initial pH = 4.5 (unadjusted), catalyst dosage = 0.5 g/L, HRT = 120 min, irradiation = three (3) UV lamps, Temperature = 25 °C.

### 3.2.4. Effect of UV Light Intensity

The intensity of the ultraviolet light directly affects the power consumption in the treatment process, and this is one of the key factors that is affecting the catalytic oxidation of the plate fixed-bed UV-Fenton reactor. For this study, the power consumption per ton of water per hour in ($Kw/m^3$) is used to express the intensity of UV light. The effect of the different UV light intensity on the degradation of TCH in the plate fixed-bed UV-Fenton

reactor is shown in Figure 7. As shown in Figure 7a–c, the two curves in the figure are the light intensity of UV radiation at the center and both ends of the UV lamp tube. As the power of the UV lamp increases, the spatial distribution of the light intensity does not change significantly, and the trend is consistent. At the same time, the further the distance from the light source, the smaller the light intensity. Since the distance between the $Al_2SiO_5$ fiberboard and the UV lamp tube in the reactor is about 3 cm, it can be seen from the figure that the light intensity ranges of the three UV lamps (4 W, 8 W, and 15 W) at 3 cm are 1.76~2.53 mW/cm$^2$, 1.84~2.81 mW/cm$^2$, and 2.38~2.98 mW/cm$^2$, respectively. In the TCH degradation test, as shown in Figure 7d, under the conditions of 4 W, 8 W, and 15 W, the removal rates of TCH after 100 min were 90.5%, 99.1%, and 99.8%, respectively. This is because the increase in the light intensity can improve the absorption of light by the solution and the catalyst and accelerate the oxidation reaction rate of TCH. Although increasing the light intensity can improve the degradation effect of TCH, it also increases the consumption of electricity, and the increase in the removal rate of TCH is less than the increase in light intensity. Therefore, lower light intensity and longer operation time can meet the processing effect and reduce the power consumption at the same time.

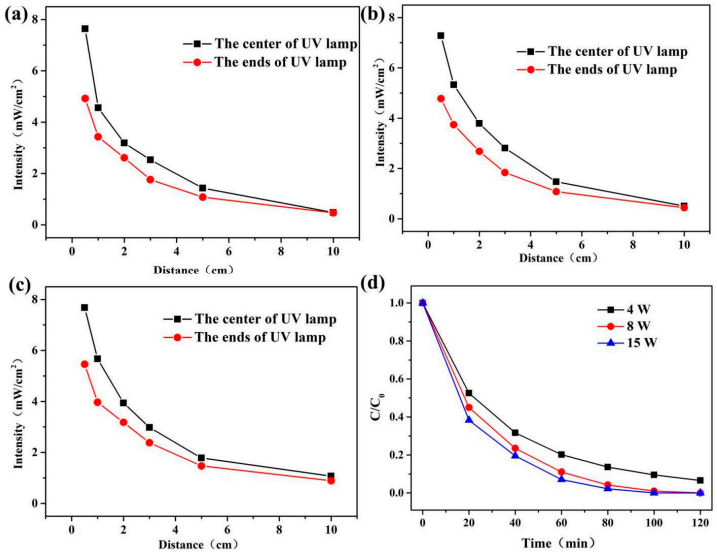


**Figure 7.** Effect of UV light intensity on TCH degradation. (**a**) the intensity of 4 W; (**b**) the intensity of 8 W; (**c**) the intensity of 15 W; (**d**) the degradation of TC under different UV light intensity. Experiment conditions: TCH concentration = 50 mg/L, initial pH = 4.5, catalyst dosage = 0.5 g/L, HRT = 120 min, $H_2O_2$ concentration = 10 m Mol/L, Temperature = 25 °C.

### 3.2.5. Effect of Hydraulic Retention Time (HRT) on TCH Degradation

The hydraulic retention time is one of the important parameters to be considered in the reactor design. From the results shown in Figure 8, with gradual reduction in hydraulic retention time, the degradation efficiency of TCH in the effluent gradually decreases. When the HRT is 180 min and the concentration of TCH in the effluent is about 2 mg/L, the removal rate of TCH in the reactor can reach more than 95%. When the HRT is gradually reduced to 120 min, the degradation efficiency of TCH decreases slightly and the removal rate of TCH is maintained at 93%. At 90 min HRT, the TCH effluent concentration of the reactor first increases rapidly and then stabilizes at about 13 mg/L and the removal rate is 70%. It can therefore be concluded that during the operation of the plate fixed-bed UV-Fenton reactor, regulating the HRT plays a vital role in the catalytic efficiency of the reactor. When the HRT is 120 min, the removal rate of TCH in the plate fixed-bed UV-Fenton reactor can achieve more than 93% efficiency.

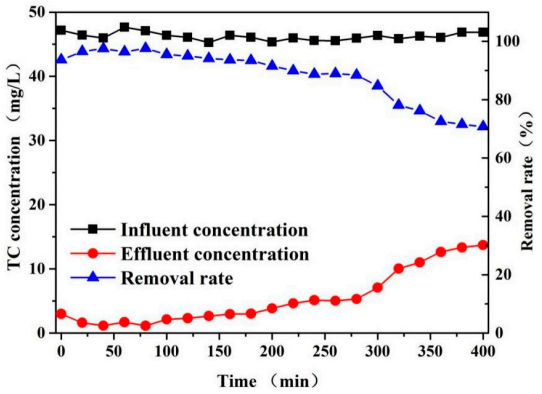


**Figure 8.** Effect of HRT on TCH degradation. Experiment conditions: TCH concentration = 50 mg/L, $H_2O_2$ concentration = 10 mmol/L, catalyst dosage = 0.5 g/L, pH = 4.5, irradiation = three (3) 6 W UV lamps, Temperature = 25 °C.

3.2.6. Effect of Different Influent TCH Concentration on the Degradation

The change in TCH concentration was studied under different concentrations (10 mg/L, 25 mg/L, 50 mg/L, and 75 mg/L) in the continuous influent and effluent and the influence of concentration change on the operation process of the reactor was investigated so as to determine the maximum load that the UV-Fenton reactor can bear. It can be seen from the results shown in Figure 9 that when the influent concentration is increased from 10 mg/L to 25 mg/L, the concentration of TCH in the effluent is lower, and the removal rate is above 96.5%. When the influent concentration was increased to 50 mg/L, it reached stability within 20 min of the reaction, the effluent concentration was maintained at about 2 mg/L, and the removal rate could reach more than 95.3%. When the influent concentration continued to increase to 75 mg/L, the effluent concentration rose slowly. After 60 min of reaction, the effluent concentration was basically stable to 11.2 mg/L, and the removal rate was 85%. The reason was that the removal rate decreased due to insufficient $H_2O_2$ in the system. It can be seen that during the operation of the reaction device, the change in the influent concentration has little effect on the removal rate of TCH, and the dynamic test device has a good impact resistance.

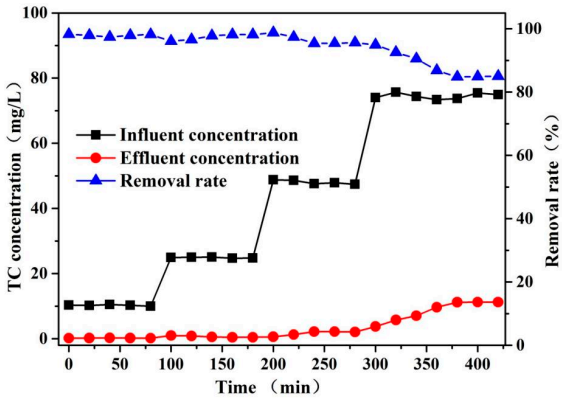


**Figure 9.** Effect of influent concentration on TCH degradation. Experiment conditions: TCH concentration = 50 mg/L, $H_2O_2$ concentration = 10 mmol/L, catalyst dosage = 0.5 g/L, pH = 4.5 (unadjusted), irradiation = three (3) 6W UV lamps, Temperature = 25 °C.

*3.3. Stability Evaluation of the Plate Fixed-Bed Reactor*

For practical industrial applications, the reactor should not only achieve a certain treatment efficiency but should also maintain an excellent stability. The stability of a reactor is one of the important indexes to evaluate its performance. The stability of the TCH degradation by the continuous operation of the reactor was investigated by means

of monitoring the continuous inlet and outlet. As shown in Figure 10, the fixed-plate UV-Fenton reactor demonstrated excellent stability during continuous operation over 24 h. When the influent concentration was 50 mg/L, the effluent concentration remained below 2.5 mg/L. The removal rate of TCH decreased from 95.3% at the start of the reaction to 94.7%, a reduction in only 0.6%, indicating no significant change in degradation efficiency.

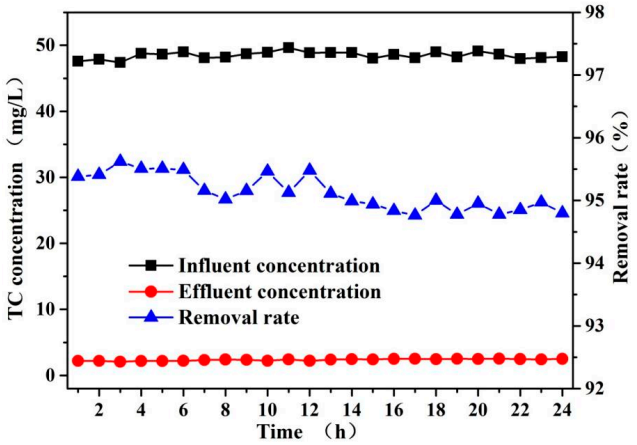


**Figure 10.** Stability test on TCH degradation in plate fixed-bed UV-Fenton reactor. Experiment conditions: TCH concentration = 50 mg/L, $H_2O_2$ concentration = 10 mmol/L, catalyst dosage = 0.5 g/L, pH = 4.5 (unadjusted), irradiation = three (3) 6 W UV lamps, Temperature = 25 °C.

### *3.4. Mechanism of Catalysts System*

#### 3.4.1. Identification of Active Species

The trapping experiment was conducted under similar experimental conditions to investigate the free radicals that play a major role in the degradation of TCH. The scavengers (250 mmol/L) were added to the reaction system. The main oxidative species detected by the trapping experiments were singlet hydroxyl (•OH), oxygen ($\bullet O_2^-$), singlet oxygen ($^1O_2$) and $h^+$ by using t-BuOH, p-benzoquinone (BQ), sodium azide, and ammonium oxalate [27–29].

The results of the active radical group inhibition experiment indicate that the main active substance involved in the degradation of TCH in Figure 11, •OH, plays a more significant role in this system. The TCH removal rate decreased to 9.11%, while the effect of $h^+$ was slightly reduced compared to the system, and the TCH removal rate decreased to 88.32%. The reason might be that the content of $TiO_2$ in the $Fe_3O_4/TiO_2@Al_2SiO_5$ catalyst is relatively low, which leads to a relatively smaller number of $h^+$ produced in the system. In contrast, the effects of $\bullet O_2^-$ and $^1O_2$ can still be ignored. The main radical group in this system remains •OH.

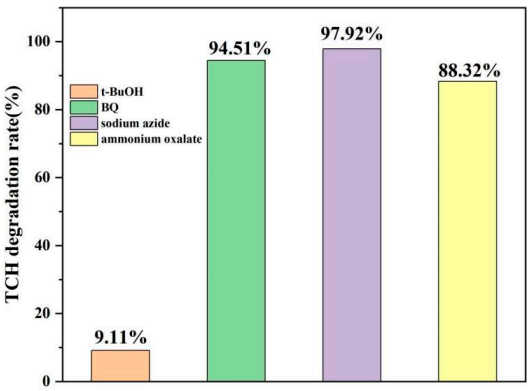


**Figure 11.** Determination of reactive species.

3.4.2. Catalytic Mechanism

On the basis of the above-mentioned experimental results, we can draw a conclusion that the $Fe_3O_4$, $TiO_2$ and $Al_2SiO_5$ fiberboard all play very important role in the UV-Fenton system for the degradation of TCH. $Al_2SiO_5$ fiberboard as a carrier enhances the dispersion and stability of the $Fe_3O_4/TiO_2$ catalyst. The specific reaction process can be seen in Equations (3)–(9), and the reaction mechanism is shown in Figure 12. $TiO_2$ possesses semiconductor conductivity and generates $h^+$ and $e^-$ under light exposure (Equation (3)). The free oxygen atoms in water combine with $e^-$ to form $\bullet O_2^-$ (Equation (4)). $H_2O$ reacts with $h^+$ to form •OH (Equation (5)). Under the action of $H_2O_2$, Fe(II) is transformed into Fe(III) and •OH (Equation (6)). Excellent charge separation prolongs the lifetime of $e^-$, enabling the reduction in Fe(III) to Fe(II) (Equation (2)). Furthermore, Fe(III) generated within the UV-Fenton system acts as an electron donor, accelerating the conversion of Fe(III) to Fe(II). This enhances the oxidative capacity of the Fenton reaction while simultaneously inhibiting electron-hole pair recombination, thereby promoting the generation of additional free radicals within the system. The enhanced efficiency of the Fe(III)/Fe(II) cycling reaction on the catalyst surface is crucial for achieving efficient TCH degradation (Equation (9)). The possible reaction mechanism is shown in Figure 12.

$$TiO_2 + h\nu \rightarrow h^+ + e^- \quad (3)$$

$$O_2 + e^- \rightarrow \bullet O_2^- \quad (4)$$

$$H_2O + h^+ \rightarrow \bullet OH \quad (5)$$

$$Fe(II) + H_2O_2 \rightarrow Fe(III) + \bullet OH + OH^- \quad (6)$$

$$\bullet OH + Fe(II) \rightarrow Fe(III) + OH^- \quad (7)$$

$$Fe(III) + H_2O_2 \rightarrow Fe(II) + H^+ \quad (8)$$

$$TCH + \bullet OH \rightarrow \text{degradation products} \quad (9)$$

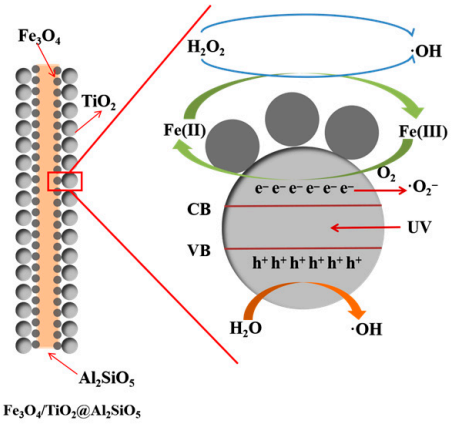


**Figure 12.** Hypothetical Reaction Mechanism Diagram.

*3.5. Degradation Pathways*

The color of TCH is determined by its chromophore, which consists of a large π-conjugated system formed by aromatic rings B, C, and D, along with their connected phenolic hydroxyl and ketone carbonyl groups (as shown in Figure 13) [30]. Due to the delocalization of electrons in the conjugated system, it can absorb light with longer wavelengths. When the wavelength of absorbed light shifts into the visible region (357 nm), the substance exhibits color. Figure 13a shows the UV-vis full-scan spectrum of UV-Fenton degradation of TCH hydrochloride catalyzed by $Fe_3O_4/TiO_2@Al_2SiO_5$.

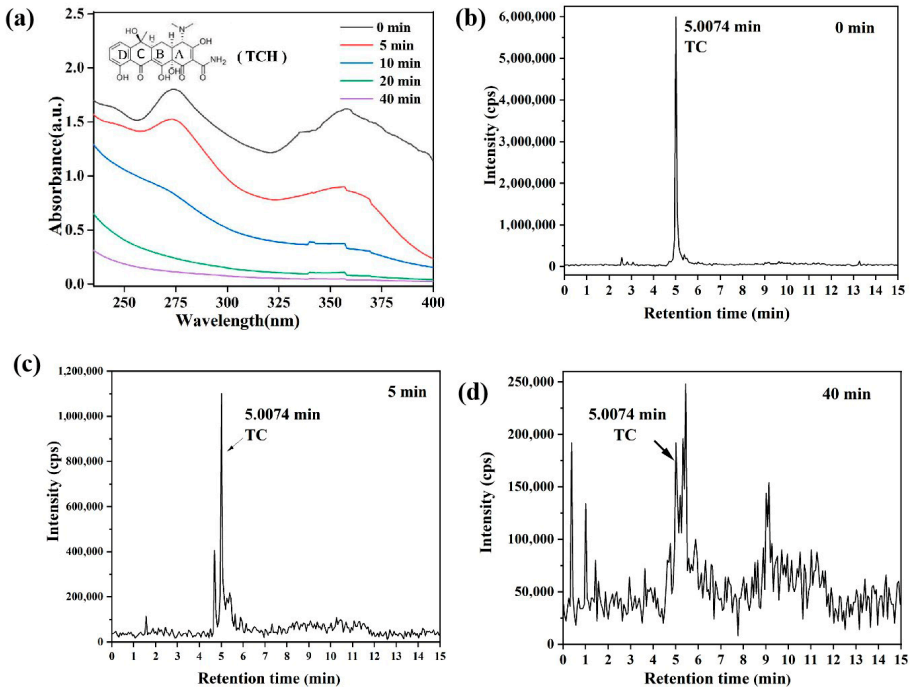


**Figure 13.** UV-vis spectra with $Fe_3O_4/TiO_2@Al_2SiO_5$ by UV-Fenton system (illustration is the structure formular of TCH) HPLC-MS/MS chromatograms for monitoring the degradation of TCH with $Fe_3O_4/TiO_2@Al_2SiO_5$ by UV-Fenton system (**a**) UV-vis spectra with $TiO_2/Fe_3O_4$@MSC by UV-Fenton system (illustration is the structure formular of TCH); HPLC-MS/MS chromatograms for monitoring the degradation of TC with $TiO_2/Fe_3O_4$@MSC by UV-Fenton system; (**b**) 0 min; (**c**) 5 min; (**d**) 40 min.

As shown in Figure 13a, prior to the catalytic reaction (0 min), tetracycline hydrochloride exhibits two distinct absorption peaks. The peak at approximately 275 nm corresponds to aromatic ring A and its associated amide and hydroxyl groups (as illustrated in Figure 13). The peak at 357 nm originates from aromatic rings B, C, D, and the extended chromophore group. As the reaction progressed, the intensities of both peaks decreased to near zero over time, indicating a gradual reduction in TCH concentration and further confirming the disruption of its conjugated structure under the UV-Fenton system. The attenuation of absorbance at 275 nm likely resulted from the destruction of the phenolic hydroxyl and amide groups within aromatic ring A of TCH and its degradation intermediates. The decay of the 357 nm visible band during the reaction resulted from the ring-opening of aromatic ring D and the subsequent disruption of its conjugated structure. Furthermore, the figure indicates that the absorption peak at 357 nm decayed faster than that at 275 nm, suggesting that aromatic rings B, C, and D, along with the extended chromophore group in the TCH molecule, were preferentially destroyed.

Figure 13b shows the chromatogram at 0 min, revealing a characteristic peak for TCH at a retention time of 5.0074 min. As the reaction progressed to 5 min in Figure 13c, the peak intensity of TCH noticeably diminished, though the peak shape remained well-defined. This indicates that a portion of TCH had been gradually degraded. Concurrently, a series of new peaks emerged, signifying the formation of new degradation products. As the reaction continued to 40 min in Figure 13d, the intensity of the TCH peak became markedly weaker than that of its reaction byproducts, confirming that TCH had been almost completely degraded.

To further understand the degradation pathway of TCH, HPLC-MS/MS and GC-MS were used to analyze the intermediate products of tetracycline in the UV-Fenton reaction system catalyzed by $Fe_3O_4/TiO_2@Al_2SiO_5$. The results are shown in Table 2.

**Table 2.** Intermediate products identified by HPLC-MS/MS.

| Products | Mass-to-Charge Ratio | Formula | Chemical Structure |
|---|---|---|---|
| TCH | 445 | $C_{22}H_{24}N_2O_8$ | 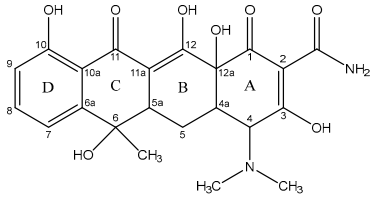 |
| P1 | 461 | $C_{22}H_{24}N_2O_9$ | 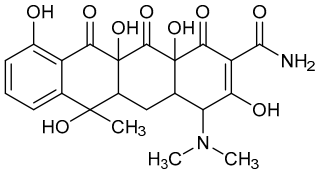 |
| P2 | 431 | $C_{21}H_{22}N_2O_8$ | 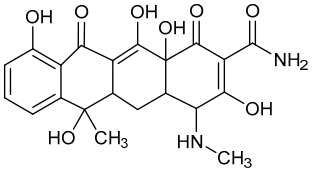 |
| P3 | 416 | $C_{21}H_{21}NO_8$ | 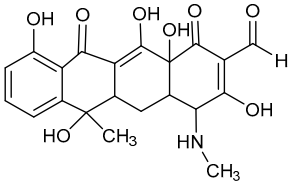 |
| P4 | 477 | $C_{22}H_{24}N_2O_{10}$ | 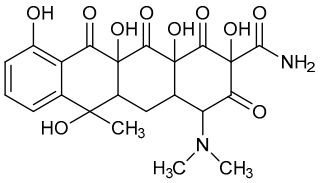 |
| P5 | 449 | $C_{20}H_{21}N_2O_{10}$ | 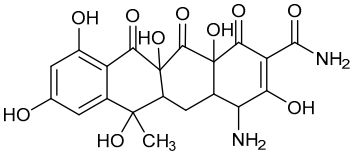 |
| P6 | 400 | $C_{21}H_{21}NO_7$ | 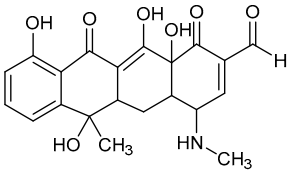 |
| P7 | 451 | $C_{20}H_{22}N_2O_{10}$ | 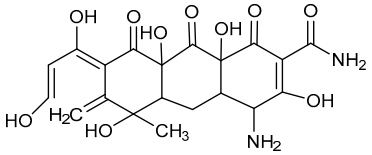 |
| P8 | 491 | $C_{22}H_{22}N_2O_{11}$ | 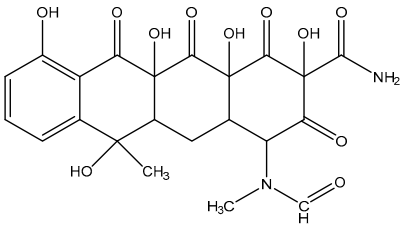 |

**Table 2.** *Cont.*

| Products | Mass-to-Charge Ratio | Formula | Chemical Structure |
|---|---|---|---|
| P9 | 468 | $C_{19}H_{17}NO_{13}$ | 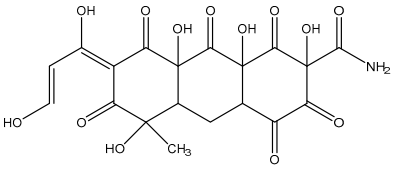 |
| P10 | 88 | $C_3H_4O$ | 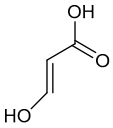 |
| P11 | 412 | $C_{16}H_{13}NO_{12}$ | 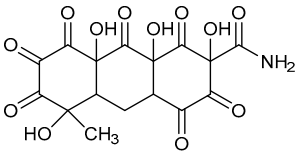 |
| P12 | 396 | $C_{15}H_9NO_{12}$ | 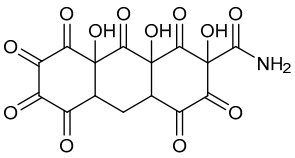 |
| P13 | 146 | $C_4H_2O_6$ | 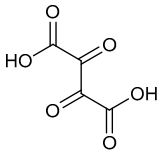 |
| P14 | 298 | $C_{11}H_7NO_9$ | 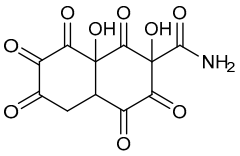 |
| P15 | 61 | $CH_3NO_2$ | 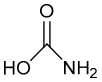 |
| P16 | 253 | $C_{10}H_4O_8$ | 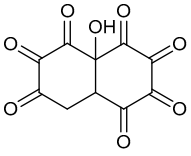 |
| P17 | 230 | $C_8H_6O_8$ | 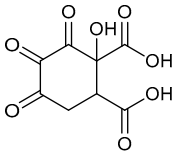 |
| P18 | 90 | $C_2H_2O_4$ | 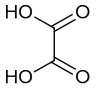 |

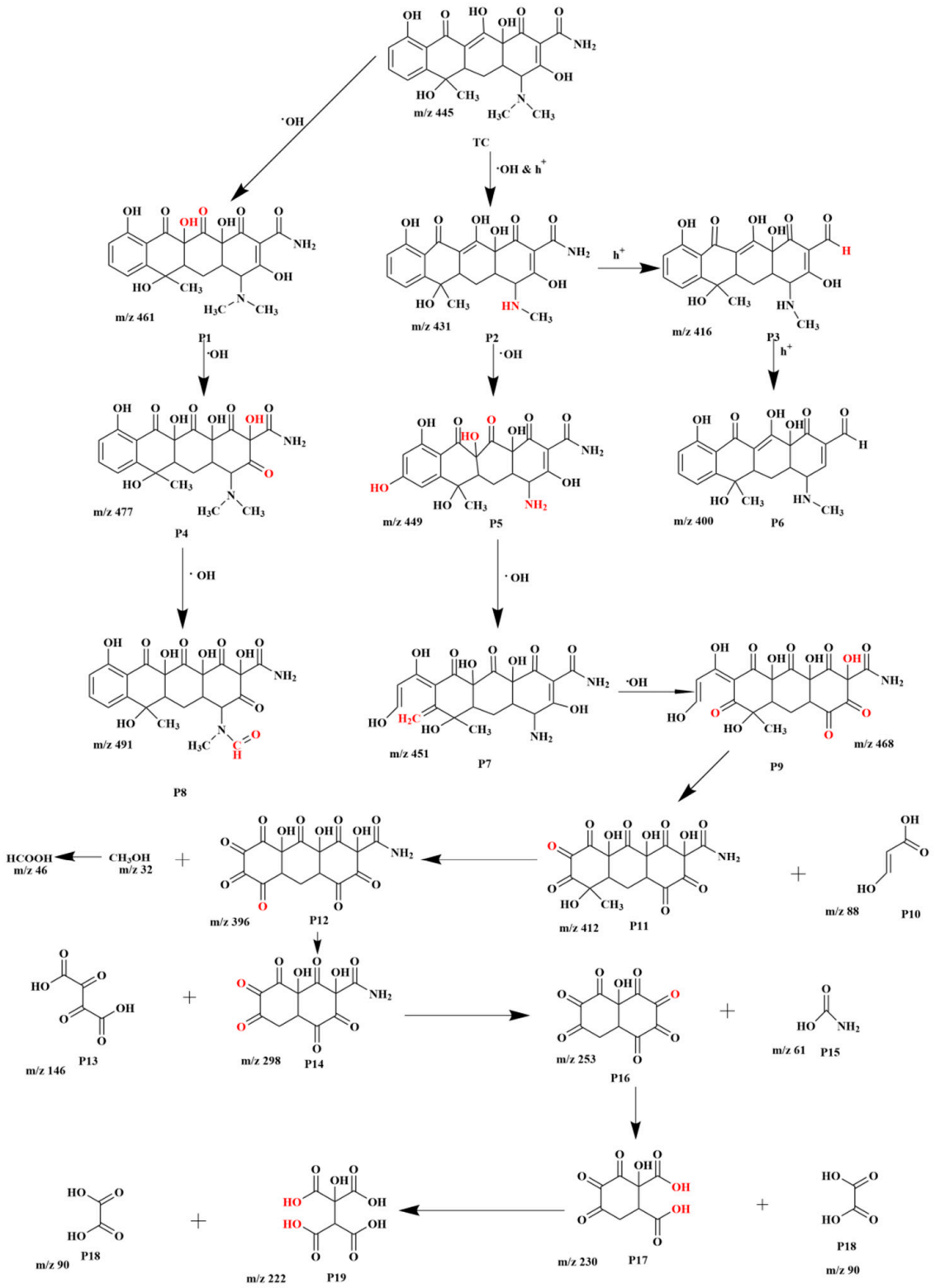


**Figure 14.** Proposed degradation pathway of TCH with $Fe_3O_4/TiO_2@Al_2SiO_5$ by UV-Fenton system.

From the results in Table 2, it can be seen that the UV-Fenton system catalyzed by $TiO_2/Fe_3O_4@Al_2SiO_5$ produced a total of 19 intermediate products. Based on the detected intermediate products, the degradation pathway of TCH was briefly analyzed, and the results are shown in Figure 14. It can be seen that one of the degradation pathways of TCH is the hydroxylation reaction of tetracycline by •OH [31], generating polar molecules with larger $m/z$ ratios than the tetracycline parent, such as intermediate products with

$m/z$ 461 and 477. The product with $m/z$ 461 is presumably formed by the addition of the C11a-C12 double bond of the tetracycline molecule followed by the rearrangement of the hydroxyl group at C12 into a carbonyl group. The product with $m/z$ 477 is produced by the further addition of •OH at the C-2 position. On this basis, •OH further attacks one methyl group of the amino group, leading to the formation of a compound with $m/z$ 491. Another degradation pathway of TCH involves the demethylation by •OH and $h^+$, which attacks the N-C bond with lower bond energy, resulting in the destruction of the N-methyl group of TCH and the generation of a substance with $m/z$ 431 [32]. On one hand, the amino group in the amide group of the polar molecule with $m/z$ 431 is destroyed to form an intermediate with $m/z$ 416, and the further destruction of the hydroxyl group produces a product with $m/z$ 400. On the other hand, demethylation and hydroxylation occur to generate a degradation product with $m/z$ 449. The aromatic ring D of this substance opens, forming a product with $m/z$ 451. Subsequently, product 6 ($m/z$ 451) undergoes demethylation, deamination, and hydroxylation to form product 9 ($m/z$ 468). The double bond at the C10-10a position of product 9 is easily attacked by •OH. When the C10-10a double bond is attacked by •OH, product 11 ($m/z$ 412) and product 10 (3-hydroxyacrylic acid, $m/z$ 88) are generated. The C6 position of product 11 is attacked by •OH, producing product 12 ($m/z$ = 396) and methanol ($m/z$ = 32). Methanol can be further oxidized to formic acid ($m/z$ = 46). The C5a and C11a positions of product 12 are attacked by •OH, generating product 14 ($m/z$ = 298) and 2,3-dioxosuccinic acid (product 13, $m/z$ = 146). •OH further attacks product 14, oxidizing it to product 16 ($m/z$ = 253) and carbamic acid (product 15, $m/z$ = 61), which is caused by the free radical attacking the C2 position. Product 16 is attacked by •OH at the C1-C2 and C3-C4 positions, forming 1-hydroxy-4,5,6-trioxocyclohexane-1,2-dicarboxylic acid (product 17, $m/z$ = 230) and oxalic acid (product 18, $m/z$ = 90). The former can be oxidized at the C5-C5a and C11a-C12 positions to generate 1-hydroxyethane-1,1,2,2-tetracarboxylic acid (product 19, $m/z$ = 222) and oxalic acid (product 18, $m/z$ = 90). These degradation products are ultimately converted into small-molecule organic compounds, $NH_4^+$, $CO_2$, and $H_2O$.

### 3.6. Toxicity Evaluation

TCH and its degradation intermediates generated during the reaction exert certain hazards and impacts on the survival and growth of aquatic animals, aquatic plants, and algae. Therefore, this study predicted the toxicity of TCH degradation intermediates using the ECOSAR program [32]. The prediction results from ECOSAR indicated that algae, fish, and green algae exhibit differences in sensitivity to TCH and its degradation intermediates, with algae showing the most significant sensitivity [33]. Acute toxicity data, as presented in the heat map of Figure 15, revealed that P1 to P10 have high toxicity to fish; P1 to P6 and P8 display extremely high toxicity to daphnids, while the remaining intermediates have low toxicity to daphnids. For green algae, P1 to P10 possess high toxicity, and the toxicity of subsequent degradation intermediates decreases. Chronic toxicity data, as observed in Figure 15, showed that all intermediates except P9, P11, P12, P13, P14, P15, P16, P17, P18, and P19 exert extremely high toxicity to daphnids. All intermediates except P9 to P19 demonstrate extremely high toxicity to fish. Regarding algae, P1 to P8 have extremely high toxicity, while the remaining chemicals are only slightly hazardous or harmless. The above analysis results indicated that the toxicity of intermediates undergoes significant changes during TCH degradation, with the product toxicity gradually decreasing.

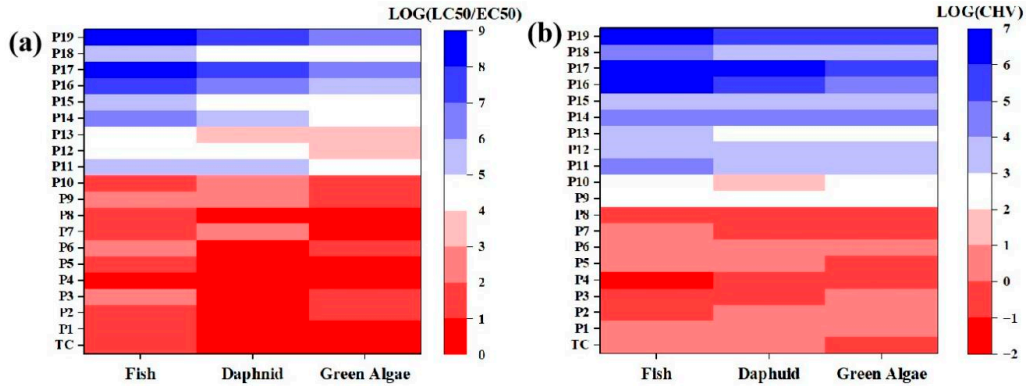


**Figure 15.** LC50, EC50, and ChV values of TCH and the detected byproducts on fish, daphnia and green algae. (**a**) acute toxicity; (**b**) chronic toxicity.

## 4. Conclusions

In this study, a new type of plate fixed-bed UV-Fenton reactor is developed and designed for prospective practical application of UV-Fenton system in antibiotic TCH wastewater. Using $Al_2SiO_5$ fiberboard as carrier, successful preparation of supported catalytic $TiO_2/Fe_3O_4@Al_2SiO_5$. The supported catalysts on fiberboard were mainly amorphous phase and the $TiO_2/Fe_3O_4$ was successfully loaded on $Al_2SiO_5$ fiberboard. The initial pH and $H_2O_2$ dosage had significant effect on the operation of reactor, followed by the hydraulic retention time, and the UV intensity. The optimum reaction conditions are influent concentration of TCH is 50 mg/L, the hydraulic retention time is 120 min, the initial pH is 4.5, the dosage of $H_2O_2$ is 10 mmol/L, and the UV light intensity is 2.36 kW/m$^3$. The removal rate of TCH subsequently achieved more than 90%. A proposed TCH degradation pathway was given according to the by-products detected by HPLC-MS/MS and GC-MS. The primary degradation pathways for TCH involve addition and substitution reactions with organic compounds through hydroxylation by •OH radicals, as well as demethylation by •OH and $h^+$, leading to the detachment of certain functional groups (such as amino, methyl, and carboxyl groups) from the TCH. Additionally, HPLC/MS-MS and GC-MS analysis identified several lower $m/z$ products, indicating that prolonged degradation can achieve complete mineralization of TCH.

**Author Contributions:** Conceptualization, X.Y.; methodology, Y.C.; data curation, Q.J.; writing—original draft preparation, X.Y.; writing—review and editing, X.Y.; funding acquisition, X.Y. All authors have read and agreed to the published version of the manuscript.

**Funding:** This research was funded by the Jilin Provincial Department of Science and Technology of China, grant number No. YDZJ202201ZYTS630.

**Data Availability Statement:** The original contributions presented in this study are included in the article. Further inquiries can be directed to the corresponding author.

**Conflicts of Interest:** The authors declare no conflicts of interest.

## References

1. Jiang, M.; Wang, X.; Han, R.; Ning, P.; Lynch, I.; Ma, J. Establishing photocatalysis-self-Fenton system over a S-scheme $Fe/Fe_2O_3@CuBi_2O_4$ for enhancing TC removal via in-situ generating $H_2O_2$ and Fe/Cu dual-metal electron cycle: Radical and non-radical pathways. *Sep. Purif. Technol.* **2025**, *354*, 128675. [CrossRef]
2. Shen, C.; He, M.; Zhang, J.; Liu, J.; Su, J.; Dai, J. Effects of the coexistence of antibiotics and heavy metals on the fate of antibiotic resistance genes in chicken manure and surrounding soils. *Ecotoxicol. Environ. Saf.* **2023**, *263*, 115367. [CrossRef] [PubMed]
3. Cevallos-Mendoza, J.E.; Cedeño-Muñoz, J.S.; Navia-Mendoza, J.M.; Figueira, F.; Amorim, C.G.; Rodríguez-Díaz, J.M.; Montenegro, M.C.B.S.M. Development of hybrid MIL-53(Al)@CBS for ternary adsorption of tetracyclines antibiotics in water: Physical interpretation of the adsorption mechanism. *Bioresour. Technol.* **2024**, *396*, 130453. [CrossRef]

4. Li, S.; Peng, L.; Yang, C.; Song, S.; Xu, Y. Cometabolic biodegradation of antibiotics by ammonia oxidizing microorganisms during wastewater treatment processes. *J. Environ. Manag.* **2022**, *305*, 114336. [CrossRef]
5. Dehghani, M.H.; Nabizadeh, R.; Ramezanian, N.; Alimohammadi, M.; Najafpoor, A.A.; Ahmadi Nasab, M.; Dehghan, A. Solar photocatalytic removal of tetracycline using bismuth oxyiodide: Intermediates identification, toxicity assessment and effect of solution matrix. *Results Eng.* **2025**, *25*, 103796. [CrossRef]
6. Liang, S.; Zhang, H.; Dai, H.; Wan, X.; Zhu, F.; Xu, Q.; Ji, W. Efficient, rapid and simple adsorption method by polydopamine polystyrene nanofibers mat for removal of multi-class antibiotic residues in environmental water. *Chemosphere* **2022**, *288*, 132616. [CrossRef]
7. Li, Q.; Tan, J.; Sha, H.; Li, K.; Li, X. Adsorption of Macrolide Antibiotics by Aged Microplastics of Different Sizes: Mechanisms and Effects. *Nanomaterials* **2025**, *15*, 467. [CrossRef]
8. Liu, M.; Wang, C.; Qi, X.-E.; Du, S.; Ni, H. Reducing residual chlortetracycline in wastewater using a whole-cell biocatalyst. *Ecotoxicol. Environ. Saf.* **2024**, *282*, 116717. [CrossRef]
9. Wang, Y.; Kang, X.; Li, Y.; Li, R.; Wu, C.; Wang, L.; Wang, C.; Yang, T.; Ge, M.; He, Z. Cobalt-loaded carbon nanofibers as magnetic catalyst for tetracycline degradation through peroxydisulfate activation: Non-radical dominated mechanism. *J. Water Process Eng.* **2024**, *57*, 104600. [CrossRef]
10. Zhang, K.; Kang, S.; Jia, R.; Wang, C. Unraveling the impact of Cu-loading in MIL-101(Fe) for markedly boosting photocatalytic PMS activation for TC degradation. *Environ. Res.* **2025**, *278*, 121664. [CrossRef] [PubMed]
11. Singh, B.; Rafiquee, M.Z.A. Kinetics of the Degradation of Tetracycline Hydrochloride by $H_2O_2$ in the Presence of Cu–$Fe_3O_4$ Nanoparticles Under Sonication. *J. Solut. Chem.* **2025**, *54*, 704–720. [CrossRef]
12. Zhang, X.; Liu, Y.; Yuan, J. Amino-functionalized Fe/Co bimetallic MOFs for accelerated Fe (III)/Fe (II) cycling and efficient degradation of sulfamethoxazole in Fenton-like system. *Front. Chem.* **2025**, *13*, 1579108. [CrossRef]
13. Du, D.; Shi, W.; Wang, L.; Zhang, J. Yolk-shell structured $Fe_3O_4$ @void@$TiO_2$ as a photo-Fenton-like catalyst for the extremely efficient elimination of tetracycline. *Appl. Catal. B* **2017**, *200*, 484–492. [CrossRef]
14. Mohamed, M.M.; Bayoumy, W.A.; Goher, M.E.; Abdo, M.H.; Mansour El-Ashkar, T.Y. Optimization of α-$Fe_2O_3$ @$Fe_3O_4$ incorporated N-$TiO_2$ as super effective photocatalysts under visible light irradiation. *Appl. Surf. Sci.* **2017**, *412*, 668–682. [CrossRef]
15. Xu, T.; Zhu, R.; Zhu, G.; Zhu, J.; Liang, X.; Zhu, Y.; He, H. Mechanisms for the enhanced photo-Fenton activity of ferrihydrite modified with $BiVO_4$ at neutral pH. *Appl. Catal. B* **2017**, *212*, 50–58. [CrossRef]
16. Deng, Y.; Xing, M.; Zhang, J. An advanced $TiO_2$ /$Fe_2TiO_5$ /$Fe_2O_3$ triple-heterojunction with enhanced and stable visible-light-driven fenton reaction for the removal of organic pollutants. *Appl. Catal. B* **2017**, *211*, 157–166. [CrossRef]
17. Deng, X.; Zhang, Q.; Zhao, Q.; Ma, L.; Ding, M.; Xu, X. Effects of architectures and $H_2O_2$ additions on the photocatalytic performance of hierarchical $Cu_2O$ nanostructures. *Nanoscale Res. Lett.* **2015**, *10*, 8. [CrossRef]
18. Ballari, M.d.l.M.; Brandi, R.; Alfano, O.; Cassano, A. Mass transfer limitations in photocatalytic reactors employing titanium dioxide suspensions. *Chem. Eng. J.* **2008**, *136*, 242–255. [CrossRef]
19. Tryba, B. Immobilization of $TiO_2$ and Fe-C-$TiO_2$ photocatalysts on the cotton material for application in a flow photocatalytic reactor for decomposition of phenol in water. *J. Hazard. Mater.* **2008**, *151*, 623–627. [CrossRef] [PubMed]
20. Mahmood, Z.; Garg, S.; Yuan, Y.; Xie, L.; Wang, Y.; Waite, T.D. Performance evaluation and optimization of a suspension-type reactor for use in heterogeneous catalytic ozonation. *Water Res.* **2024**, *254*, 121410. [CrossRef] [PubMed]
21. Chandekar, K.V.; Yadav, S.P. Comprehensive study of $MFe_2O_4$ (M=Co, Ni, Zn) nanostructures prepared by co-precipitation route. *J. Alloys Compd.* **2023**, *960*, 170838. [CrossRef]
22. Yao, J.; Yan, J.; Huang, Y.; Li, Y.; Xiao, S.; Xiao, J. Preparation of $ZnFe_2O_4$/α-$Fe_2O_3$ Nanocomposites from Sulfuric Acid Leaching Liquor of Jarosite Residue and Their Application in Lithium-Ion Batteries. *Front. Chem.* **2018**, *6*, 442. [CrossRef] [PubMed]
23. Uthiravel, V.; Narayanamurthi, K.; Raja, V.; Anandhabasker, S.; Kuppusamy, K. Green synthesis and characterization of $TiO_2$ and Ag-doped $TiO_2$ nanoparticles for photocatalytic and antimicrobial applications. *Inorg. Chem. Commun.* **2024**, *170*, 113327. [CrossRef]
24. Shi, C.; Wang, M.; Zhang, Z.; Zhou, H.; Hu, P.; He, L.; Liu, X.; Cai, H.; Pang, Z. Novel $Fe_3O_4$@$TiO_2$@PB ternary composites for photocatalytic magnetorheological polishing of ceramic dentures and photocatalytic degradation of pollutants. *Surf. Interfaces* **2025**, *70*, 106849. [CrossRef]
25. Nie, M.; Li, Y.; Li, L.; He, J.; Hong, P.; Zhang, K.; Cai, X.; Kong, L.; Liu, J. Ultrathin iron-cobalt oxide nanosheets with enhanced $H_2O_2$ activation performance for efficient degradation of tetracycline. *Appl. Surf. Sci.* **2021**, *535*, 147655. [CrossRef]
26. Yu, X.; Lin, X.; Feng, W.; Li, W. Effective Removal of Tetracycline by Using Bio-Templated Synthesis of $TiO_2$/$Fe_3O_4$ Heterojunctions as a UV–Fenton Catalyst. *Catal. Lett.* **2019**, *149*, 552–560. [CrossRef]
27. Liu, H.; Chen, Y.; Yu, Z.; Yang, G.; Song, Y.; Wang, J.; Chen, J.; Jiang, J. Metal-doped Fe@MXene/CdS Schottky junction photocatalysts for efficient $H_2O_2$ generation and self-Fenton degradation of TC. *J. Alloys Compd.* **2025**, *1037*, 182302. [CrossRef]

28. Yu, N.; Ma, H.; Wen, Z.; Zhang, W.; Chen, J.; Yuan, Y.; Zhou, L. Bacteria-based biochar as a persulfate activator to degrade organic pollutants. *Environ. Sci. Pollut. Res.* **2023**, *30*, 83289–83301. [CrossRef]
29. Han, Y.; Gan, L.; Gong, H.; Han, J.; Qiao, W.; Xu, L. Photoactivation of peroxymonosulfate by wood pulp cellulose biochar/g-$C_3N_4$ composite for diclofenac degradation: The radical and nonradical pathways. *Biochar* **2022**, *4*, 35. [CrossRef]
30. Xiong, W.; Gao, Y.; Wu, X.; Hu, X.; Lan, D.; Chen, Y.; Pu, X.; Zeng, Y.; Su, J.; Zhu, Z. Composite of Macroporous Carbon with Honeycomb-Like Structure from Mollusc Shell and $NiCo_2O_4$ Nanowires for High-Performance Supercapacitor. *ACS Appl. Mater. Interfaces* **2014**, *6*, 19416–19423. [CrossRef]
31. Liu, J.; Li, X.; Chu, Y.; Yuan, L.; Lv, R.; Zhang, W. An autocatalytic Fe(III)/$H_2O_2$ Fenton-like process triggered by tetracycline: The overlooked effect of quinone intermediates. *Chem. Eng. J.* **2023**, *475*, 146035. [CrossRef]
32. Zhang, H.; Wang, Z.; Li, R.; Guo, J.; Li, Y.; Zhu, J.; Xie, X. $TiO_2$ supported on reed straw biochar as an adsorptive and photocatalytic composite for the efficient degradation of sulfamethoxazole in aqueous matrices. *Chemosphere* **2017**, *185*, 351–360. [CrossRef] [PubMed]
33. Li, F.; Sun, G.; Fan, T.; Zhang, N.; Zhao, L.; Zhong, R.; Peng, Y. Ecotoxicological QSAR modelling of the acute toxicity of fused and non-fused polycyclic aromatic hydrocarbons (FNFPAHs) against two aquatic organisms: Consensus modelling and comparison with ECOSAR. *Aquat. Toxicol.* **2023**, *255*, 106393. [CrossRef] [PubMed]